Journal of Zhejiang University-SCIENCE A 2026 27(3):231-245
www.jzus.zju.edu.cn; www.springer.com/journal/11582
E-mail: jzus_a@zju.edu.cn

Research Article
https://doi.org/10.1631/jzus.A2500203

Check for updates

Monte Carlo simulation method for estimating the fine rattler fraction in large-ratio binary mixtures

Jing WANG[1,2], Changyu SHI[1], Daosheng LING[1,2]✉

[1]*MOE Key Laboratory of Soft Soils and Geoenvironmental Engineering, Institute of Geotechnical Engineering, Zhejiang University, Hangzhou 310058, China*
[2]*Center for Hypergravity Experimental and Interdisciplinary Research, Zhejiang University, Hangzhou 310058, China*

Abstract: Reliable estimation of the fine particle rattler fraction is crucial for understanding the structural and mechanical responses of binary granular systems with large size ratios. However, such estimation is challenged by the general inability to obtain interparticle contact force information directly from experimental images and by the lower accuracy of positional and size identification of fine particles compared with coarse particles. To address these challenges, in this study, we focused on 2D bidisperse granular assemblies with large size ratios (α=7, 9, 12, and 16) and developed an approach based on Monte Carlo simulation (MCS) that relies solely on the size and positional information of coarse particles, avoiding the need for force-resolved computations. The performance of the method was evaluated against experimental measurements and discrete element method (DEM) simulations. The MCS-based predictions show close agreement with experimental results, with a slight overall overestimation. At low fines content, the approach tends to overestimate the fine particle rattler fraction relative to DEM results, whereas at higher fines content, it underestimates the rattler fraction. Overall, the proposed MCS-based approach enables robust and relatively accurate estimation of the fine particle rattler fraction. This study provides a practical framework for predicting the rattler fraction, contributes to advancing both experimental analysis and theoretical modeling in granular physics, and demonstrates the conceptual extendibility of the MCS framework to more complex 3D packings.

Key words: Granular materials; Rattlers; Fines content; Size ratio; Discrete element method (DEM); Monte Carlo

1 Introduction

Binary granular soil mixtures, such as sand-silt and gravel-sand mixtures, are widely used in geotechnical structures, including foundations, rockfill dams, and railway ballasts, where their macromechanical properties are essential for structural stability. The macroscopic behavior of these materials is closely linked to their particle-scale interactions. A jammed granular material consists of two coexisting subsets of particles: non-rattlers and rattlers (Behringer and Chakraborty, 2019). A particle is considered a rattler if it has too few contacts to contribute to the mechanical stability of the packing (Santos et al., 2020; Srivastava et al., 2021). Specifically, a particle is typically identified as a rattler if its number of contacts z_i falls below a critical threshold c ($z_i<c$), where c depends mainly on the system's dimensionality and the presence of interparticle friction. Table 1 summarizes representative values of c reported in previous studies under various dimensional and frictional conditions. For 2D systems, there is a broad consensus that c=3 for frictionless particles and c=2 for frictional ones. In contrast, for 3D systems, different studies have adopted various values of c even under the same frictional condition.

The number of rattlers directly reflects the mechanical redundancy of a granular system (Huang et al., 2014), and their undifferentiated inclusion can obscure meaningful statistical analyses. Many studies exclude rattlers when computing structural or mechanical metrics. Thornton (2000), Biazzo et al. (2009), Lin et al. (2023), and Ling et al. (2024) excluded rattlers when calculating the average coordination number. Similarly, Zhang et al. (2010) and Berzi and Vescovi (2021) considered only non-rattler particles when evaluating

✉ Daosheng LING, dsling@zju.edu.cn
Daosheng LING, https://orcid.org/0000-0002-0604-1175

Received May 21, 2025; Revision accepted Sept. 9, 2025;
Crosschecked Jan. 16, 2026; Online first Mar. 10, 2026

Table 1 Critical coordination number c for rattler identification under different dimensionalities and friction conditions reported in previous studies

Reference	Dimensionality	Friction	c
Babu et al. (2023)	2D	N	3
Petit and Sperl (2025)	2D	N	3
Newhall (2025)	2D	N	3
Majmudar et al. (2007)	2D	Y	2
Jiang et al. (2024)	2D	Y	2
Lee et al. (2025)	2D	Y	2
Lee and Hurley (2025)	2D	Y	2
Kumar et al. (2016)	3D	N	4
Yoshii and Otsuki (2025)	3D	N	4
Santos et al. (2020); Srivastava et al. (2021)	3D	N	3
Thornton (2000)	3D	Y	2
Thakur and Penumadu (2021)	3D	Y	2
Santos et al. (2020); Srivastava et al. (2021)	3D	Y	2
Xu et al. (2021)	3D	Y	2
Redaelli and di Prisco (2019)	3D	Y	2
Wautier et al. (2019)	3D	Y	1

N and Y indicate frictionless and frictional systems, respectively

fabric tensors. Huang et al. (2014) and Duverger et al. (2021) treated rattlers as voids when determining the critical state void ratio, thereby recovering the classical form of the critical state line, in which the void ratio decreases with increasing confining pressure. Moreover, Tejada et al. (2025) corrected the computation of the mean macroscopic stress by scaling the stress tensor $\boldsymbol{\sigma}_{ij}$ by $1/(1-\eta_r)$, where η_r denotes the rattler fraction, defined as the ratio of rattler number to the total number of particles.

Although often excluded to reduce statistical distortion, recent studies have highlighted the potentially constructive roles of rattlers in granular mechanics. For example, Wautier et al. (2019) conducted a series of drained triaxial loading simulations using the discrete element method (DEM) with various rattler contents and found that rattlers help stabilize the granular skeleton. Similarly, Hu et al. (2024) showed that rattlers provide lateral support to force chains, thereby enhancing shear strength under confining pressure.

These contrasting roles underscore the importance of accurately estimating η_r. Previous research has shown that η_r is affected by several factors, including particle size distribution (Prasad et al., 2017; Maher and Torquato, 2024), confining pressure (Huang et al., 2014; Duverger et al., 2021; Hu et al., 2024), and interparticle friction (Huang et al., 2014; Srivastava et al., 2021). For example, Prasad et al. (2017) simulated random, close-packed binary mixtures of spheres and found that the fine rattler fraction η_r^f (rattlers among fine particles) increases with the size ratio α (coarse–to–fine radius ratio) at a fixed fines content f_c (volume fraction of fine particles) and decreases with f_c at fixed α. Notably, when $\alpha \geqslant 5.75$ and $f_c<20\%$, most fine particles are unjammed, causing their η_r^f to approach 100%. In contrast, coarse particles generally remain jammed across all f_c levels because of their relatively large size. Consequently, fine rattlers become the dominant contributor to the total rattler number in systems with large α and low f_c, making their estimation critical for understanding structural and mechanical responses. For 2D isotropic packings with α up to about 2, Jiang et al. (2024) showed that η_r can be linearly approximated using the mean cell order, regardless of the particle shape.

While the DEM can determine all interparticle contact forces through force-resolved computations and thereby achieve high predictive accuracy in η_r, such mechanical information is generally not directly obtainable from experimental techniques such as X-ray computed tomography (Xia et al., 2017; Cheng and Wang, 2018) or simple optical imaging (Wang et al., 2026). Under a fixed imaging resolution, coarser particles are generally identified with higher accuracy than finer ones (Li et al., 2025). Because experimental images lack direct contact force information, determining whether two particles are actually in contact based solely on size and positional information is inherently challenging (Xia et al., 2017), and the relatively low identification accuracy of fine particles further increases the difficulty of resolving contacts involving them. Although some studies have attempted to infer contact forces indirectly using multi-objective optimization algorithms (Hurley et al., 2016a, 2016b), this was beyond the scope of the present study.

Owing to the inherently stochastic nature of pore networks and particle arrangements, estimating η_r represents a typical uncertainty quantification problem. The Monte Carlo simulation (MCS) method, widely used for uncertainty analysis (Elishakoff, 2003), has been extensively applied in geotechnics (Wang et al., 2010; Wang, 2011; Zhang et al., 2022; Gao et al., 2023).

This enables the quantitative assessment of system responses under uncertainty through large-scale stochastic sampling (Hu and Wang, 2020; Li and Wang, 2023).

Although 3D granular assemblies better represent real-world systems, they also involve more complex contact networks. In contrast, 2D packing offers a more tractable framework for investigating particle-scale packing structures and estimating η_r due to its geometric simplifications.

To address the challenges posed by the general inability to obtain interparticle contact force information directly from experimental images of granular packings, as well as the lower positional and size identification accuracy of fine particles compared to coarse particles—both of which hinder the estimation of η_r^f—in this study, we framed the estimation of η_r^f as an uncertainty quantification problem. Focusing on 2D bidisperse granular assemblies with large size ratios (α=7, 9, 12, and 16), we developed an MCS-based approach that relies exclusively on the size and positional information of coarse particles, without requiring force-resolved computations.

2 Methodology

In this paper, we propose an MCS-based method for estimating the proportion of fine rattlers in binary mixtures. The basic conceptual framework involves first determining the void size distribution within the coarse particle assembly, followed by placing fine particles in these voids and identifying those that meet the floating (rattler) criteria. The overall procedure is illustrated in Fig. 1 and includes the following five steps: (1) extracting the inscribed void size distribution from the coarse particle assembly via Delaunay tessellation, (2) adjusting the inscribed void circle size to match the maximum packing density, (3) classifying the adjusted void circles based on the maximum number of fine particles that they can accommodate, (4) calculating and updating the selection weight of each void category for random fine particle placement, and (5) identifying fine rattlers as those within voids that do not exceed their maximum capacity. This process is repeated 1000 times to compute the average fine rattler fraction η_r^f. The following subsections elaborate on each step.

2.1 Characterization of inscribed void size distribution by Delaunay tessellation

The weighted Delaunay tessellation-based algorithm, originally proposed by Al-Raoush et al. (2003) and Reboul et al. (2008), enables the evaluation of void spaces located within tetrahedra and constrictions on tetrahedral faces, where the constriction size is defined as the diameter of the largest empty disc that can fit between the three particles forming the face in numerically generated assemblies of 3D polydispersed spheres based on known particle positions and radii (Fig. 2a). In our study, we adapted this approach to a 2D granular system, where the packing domain was partitioned using Delaunay triangulation. Each triangle connects

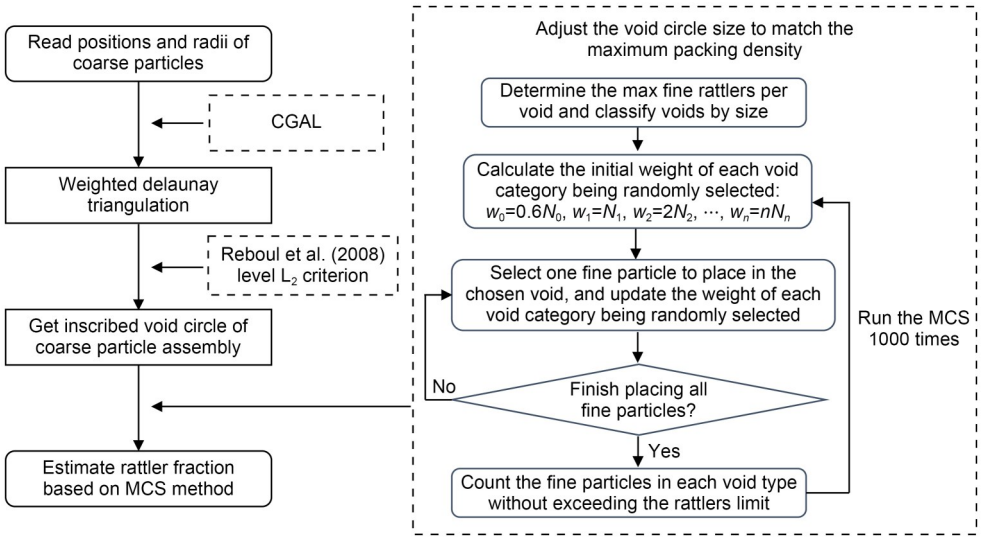

Fig. 1 Calculation procedure for the proposed MCS-based method

the centroids of three neighboring particles (Fig. 2b), and triangulation is implemented using the regular Delaunay algorithm from the Computational Geometry Algorithms Library (CGAL) (CGAL, 2024). For each triangle, we then compute an inscribed void circle tangent to the three surrounding particles joined by the triangle under consideration, rather than the inscribed circle of the geometric triangle itself, as illustrated by the blue-line circles in Fig. 3. The radius of this circle provides a useful estimate of local void size (Bryant et al., 1993; Reboul et al., 2008; Nguyen et al., 2021).

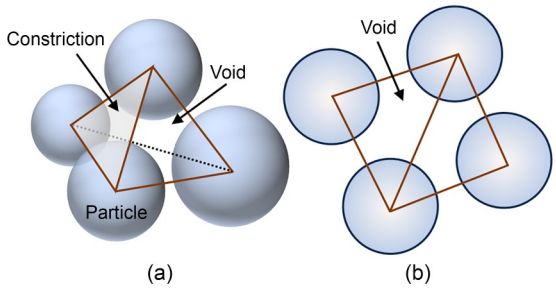

Fig. 2 Illustration of Delaunay cells: (a) 3D Delaunay cell (the tetrahedron is built from the centers of four neighboring particles; the void corresponds to the volume inside the tetrahedron, while the constrictions are associated with the faces of the cell, one of which is shaded in the figure); (b) 2D Delaunay cell (the triangulation is built from three neighboring particles)

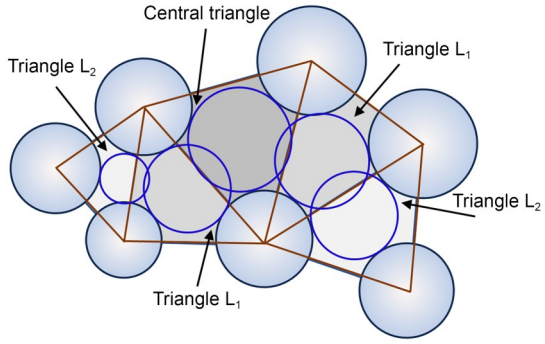

Fig. 3 Schematic diagram of adjacent triangles under the L_1 and L_2 merging criteria based on Reboul et al. (2008, 2010) (adapted from Nguyen et al. (2021)). L_2 criterion includes the central triangle, its direct neighbors (triangle L_1), and their neighbors (triangle L_2). Note that L_1 set is a subset of L_2 set

To prevent the over-segmentation of voids, Reboul et al. (2008, 2010) introduced two merging criteria, L_1 and L_2. The L_1 criterion considers a central triangle and its immediate neighbors (triangles labeled L_1 in Fig. 3), while the L_2 criterion extends this by including the next-nearest neighbors, i.e., the neighbors of the L_1 triangles (triangles labeled L_2 in Fig. 3). Merging decisions are based on the relative overlap γ, defined as $\gamma=\frac{\delta}{\min(d_i, d_j)}\in[0, 1]$, where δ is the overlap between the void circles and d_i and d_j are their respective diameters. If γ exceeds the user-specified threshold γ^{th}, the adjacent triangles are merged into one. The selection of γ^{th} is somewhat subjective: for instance, Al-Raoush et al. (2003), Shire et al. (2013), and Shire and O'Sullivan (2016) used a 50% overlap threshold, whereas Sufian et al. (2015) adopted a stricter criterion by setting $\gamma^{th}=0$, effectively disallowing any overlap. More recently, Nguyen et al. (2021) proposed a merging method with minimal dependence on γ^{th}, which yielded results comparable to those obtained using the L_2 criterion with $\gamma^{th}=0$. This consistency across methodologies supports the use of the L_2 criterion with zero overlap as a robust and objective approach for void space characterization.

Consequently, in this study, we adopted the L_2 criterion with $\gamma^{th}=0$ to ensure consistent void identification while minimizing the subjective influence during merging. The original code developed by Shire et al. (2013) for computing the constriction size distributions in 3D was modified to suit 2D systems, preserving the core-merging logic. Following Roblee et al. (1958), Reyes and Iglesia (1991), and Reboul et al. (2008), the analysis domain excludes boundary regions within a lateral distance of two coarse particle diameters to mitigate edge effects. Based on this framework, the distribution of inscribed void circle sizes is determined from the known radii and positions of coarse particles.

2.2 Adjusting the inscribed void size

Because inscribed void circles underestimate the actual void sizes arising from irregular pore shapes, they consequently underestimate the number of fine particles that can occupy the voids (Reboul et al., 2008). As illustrated in the lower right corner of Fig. 4a, the actual void can accommodate three fine particles, whereas the corresponding inscribed void circle (upper-right) permits only one. In contrast, the void area-equivalent circle method, which assumes that voids are completely filled by fine particles (i.e., packing density $\varphi=1$), tends to overestimate void capacity (Reboul et al., 2008), as illustrated in Fig. 4b. To strike a balance

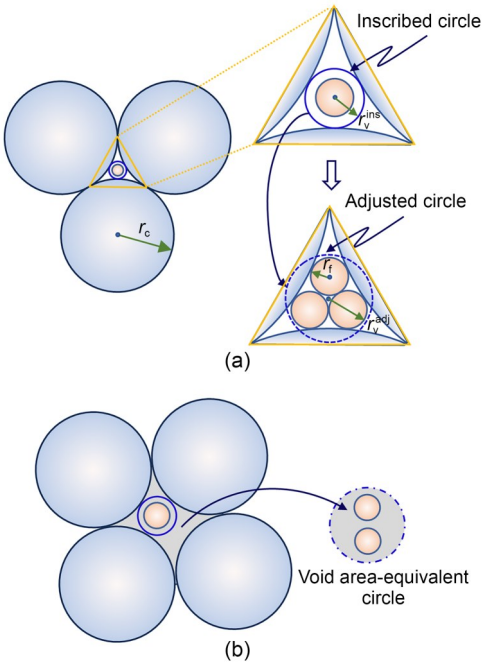

Fig. 4 Schematic illustration of void size adjustment methods: (a) underestimation of the maximum number of fine particles using the inscribed circle method, where r_c is the radius of coarse particles and r_f is the radius of fine particles; (b) overestimation of the maximum number of fine particles using the void area-equivalent circle method

between these two extremes, the radius of each inscribed void circle is adjusted such that the total void space corresponds to the maximum packing density φ_{max} of a binary mixture with a specific size ratio. This reference value reflects the densest achievable configuration under idealized conditions and provides physically meaningful normalization. This adjustment is formulated as follows:

$$\varphi_g+\pi\sum\left(sr_v^{ins}\right)^2=\varphi_{max}, \tag{1}$$

where r_v^{ins} is the original inscribed void radius obtained in Section 2.1, s is the size correction factor, and φ_g is the packing density of coarse particles, which is defined as the ratio of the total area of coarse particles to the total area of the system. Thus, the adjusted void radius is given by $r_v^{adj}=sr_v^{ins}$ as indicated by the dashed circle on the lower right side of Fig. 4a. The value of φ_{max} is determined using the 3-parameter particle packing model proposed by Kwan et al. (2013), which incorporates both filling and embedment mechanisms. Once the minimum void ratio e_{min} is known, φ_{max} can be computed as follows:

$$\varphi_{max}=1/(1+e_{min}). \tag{2}$$

Fig. 5 compares the void ratio e as a function of the fines content f_c for binary mixtures with size ratios α=7 and 9 obtained from experiments (Wang et al., 2026) and α=12 and 16 obtained from DEM simulations (detailed in Section 3.2), with corresponding theoretical predictions. The theoretical results show good agreement with both experimental and simulation data across the full range of size ratios considered. At low f_c, e decreases as f_c increases. When e reaches its minimum e_{min}, fine particles fully occupy the inter-aggregate voids, representing the transitional or threshold fines content (Lade et al., 1998; Yang et al., 2006). Beyond this point, further increases in f_c lead to an increase in e, indicating the opposite trend. The corresponding threshold fines content f_c^{th}, minimum void ratio e_{min}, and computed φ_{max} values calculated in this study are summarized in Table 2.

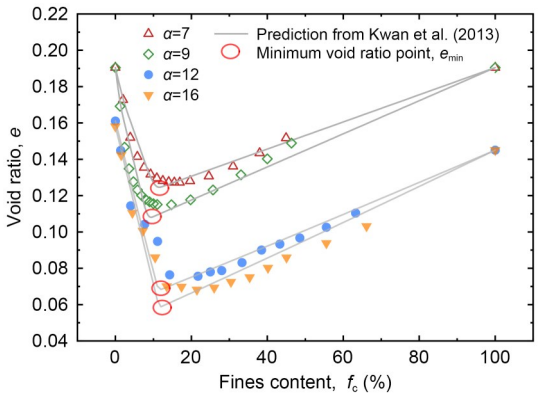

Fig. 5 Comparison of predicted and measured void ratios for binary mixtures with different size ratios α

Table 2 Threshold fines content, minimum void ratio, and maximum packing density for different size ratios calculated

Size ratio, α	Threshold fines content, f_c^{th} (%)	Minimum void ratio, e_{min}	Maximum packing density, φ_{max}
7	11.57	0.1249	0.8890
9	9.16	0.1070	0.9033
12	11.31	0.0663	0.9378
16	11.67	0.0568	0.9463

2.3 Classification of adjusted void circles

The best known packings of equal circles in a circle database (Otto von Guericke University Magdeburg,

2025a) provides optimal configurations for placing equal-sized circles within a larger enclosing circle, along with the maximum number of such circles that can be accommodated for various radius ratios. Here, the radius ratio is defined as the ratio of the adjusted void circle radius r_v^{adj} to the fine particle radius r_f. The number of fine particles that can be accommodated increases in a stepwise manner with r_v^{adj}/r_f within the range [0, 3.81] (Fig. 6a). For example, a ratio of 2.41 permits a maximum of four fine particles within the void circle. Based on this relationship, the adjusted void circles are classified according to their maximum fine-particle capacities. For each capacity level, the number of corresponding voids is counted—for instance, N_1 and N_4 represent the numbers of voids that can accommodate one and four fine particles, respectively (Fig. 6b). This classification forms the basis for the subsequent calculation of the selection weights for the Monte Carlo placement of the fine particles.

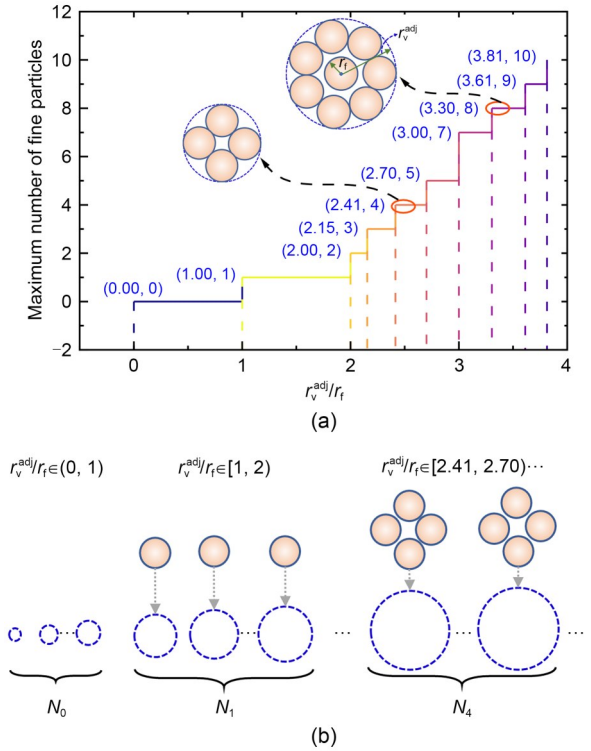

Fig. 6 Schematic diagram of classifying adjusted void circles: (a) relationship between the maximum number of equal-sized fine particles that can be accommodated and the ratio of the adjusted void circle radius to the fine particle radius (r_v^{adj}/r_f); (b) classification of adjusted void circles according to the maximum number of fine particles they can hold, where N_i denotes the number of void circles that can accommodate *i* fine particles

2.4 Initial weight calculation and update of void circles with fine particles

To account for the influence of void size and frequency on the probability of selecting a void for fine particle placement, the initial weight assigned to each void category is defined as $w_i = iN_i$ (Fig. 7a). For small voids where $r_v^{adj}/r_f \in (0, 1)$, a scaling factor of 0.6 is applied to reflect their reduced likelihood of being selected. Accordingly, the weight for this group is set as $w_0 = 0.6N_0$. This factor was optimized to match the experimental observations and simulated results (Section S1 of the electronic supplementary materials (ESM)).

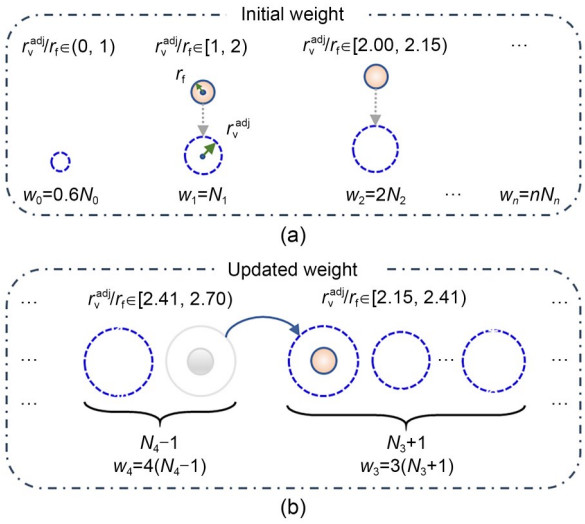

Fig. 7 Schematic illustration of the weight assignment and update process for void circles during fine particle placement: (a) initial weight calculated as the product of the maximum capacity and the number of corresponding void circles; (b) weight update mechanism as fine particles are sequentially placed, with void circles transitioning between categories based on the remaining capacity

The weights are updated dynamically during the MCS. When a fine particle is placed into a void, the number of voids in that category is reduced by one, whereas the count in the next lower category is increased by one (Fig. 7b). The corresponding weights are then recalculated to reflect the updated void circle number distribution. This process is repeated until all fine particles within the valid analysis zone are placed. The total number of fine particles in the assembly is multiplied by the area fraction of the valid region to estimate the number of fine particles within the valid zone. This region excludes a boundary zone extending

inward from the edges by a distance of two coarse particle diameters, as defined in Section 2.1. For each void circle, if the number of fine particles placed does not exceed the maximum void capacity, the particles are classified as rattlers. The total number of rattlers is recorded for each MCS. As shown in Fig. 8, the predicted η_r^f stabilizes with increasing MCS runs, based on the case of α=7 and f_c=2%, which corresponds to one of the lowest fine particle counts (N_f) among all cases considered in the experiments of Wang et al. (2026) (N_f=158). When this total fine particle number (i.e., number of runs×N_f) exceeds about 1580, the statistical variation in η_r^f falls below 1%, with values confined within a narrow range between 0.71 and 0.72. Based on this convergence behavior, 1000 was conservatively adopted as the number of MCS runs needed to ensure statistical reliability of the estimated average η_r^f for all binary mixtures.

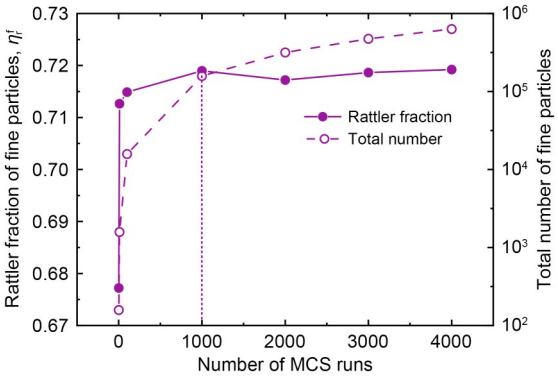

Fig. 8 Convergence behavior of the fine rattler fraction with increasing numbers of MCS runs for the binary mixture with α=7 and f_c=2%

3 Comparison of MCS-based results with experiments and simulations

3.1 Comparison with experimental data

Fig. 9 compares the fine rattler fractions η_r^f estimated using the MCS-based method with the experimental results from Wang et al. (2026) for binary mixtures with size ratios of α=7 and 9 over a range of fines contents f_c. Specifically, a series of 2D dense binary packing optical experiments with size ratios α=3, 5, 7, and 9 were conducted using colored polyoxymethylene (POM) disks of fixed thickness. The mixtures were manually prepared in a square perspex

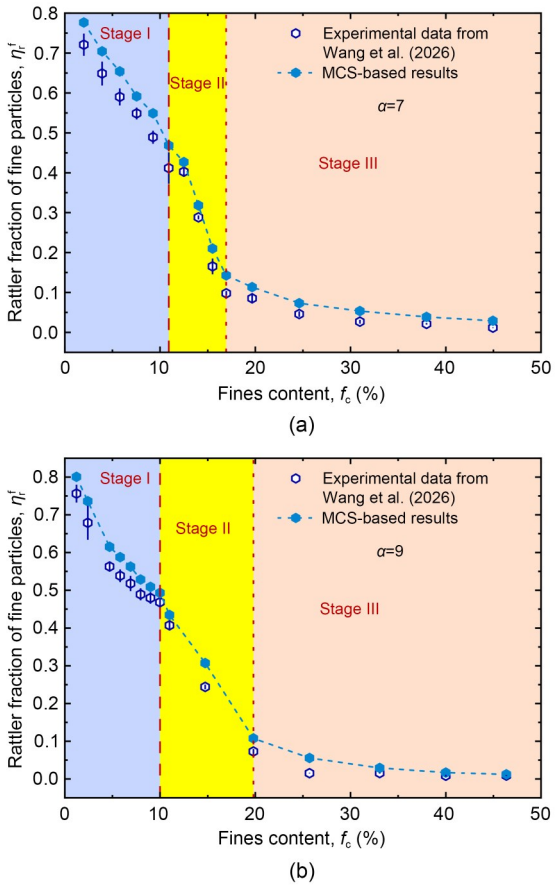

Fig. 9 Comparison of MCS-based and experimental rattler fractions for the two size ratios: (a) α=7; (b) α=9. Error bars indicate the standard error of the mean

frame placed horizontally on a glass plate to eliminate vertical pressure gradients. Each packing was constructed under high-density conditions, with all four rigid boundaries applying compressive forces to generate a jammed particle network. High-resolution images were processed using Hough transform-based detection and a distance-based contact criterion. Rattlers are defined in the experiments as particles with fewer than three contacts. Overall, the MCS-based estimates showed good agreement with the experimental observations, although they tended to slightly overestimate η_r^f. This deviation arises mainly from the idealized assumption in the MCS method: all fine particles within a void circle are treated as rattlers if their number does not exceed the maximum capacity of the circle. In practice, some of these particles may become mechanically stable due to local geometric constraints, leading to lower actual rattler counts. For instance, Fig. 10 illustrates a case where three fine particles are

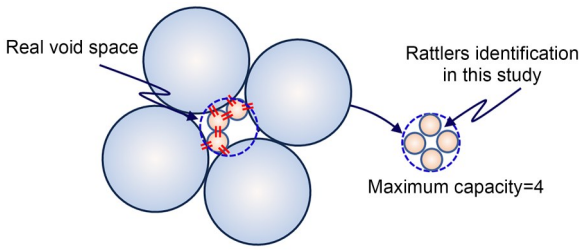

Fig. 10 Diagram of the discrepancy in rattler identification between actual void spaces and the maximum circle capacity assumption used in the MCS method. The dashed circle represents the adjusted void circle, while short red double-solid lines denote contacts between particles and their neighbors

already mechanically stable in a real void, whereas the corresponding adjusted void circle under the MCS assumption requires at least five particles to achieve a non-rattler configuration.

In addition, the discrepancy is partly attributed to the contact detection criterion used in experimental image processing. Specifically, two particles are identified as being in contact if the distance between their centers satisfies a threshold-based condition. As f_c increases, fine particles become more densely packed (Fig. 11), making the system more prone to registering apparent contacts between particles that are not actually touching when a fixed threshold is used. This leads to an underestimation of η_r^f when applying a coordination-based criterion.

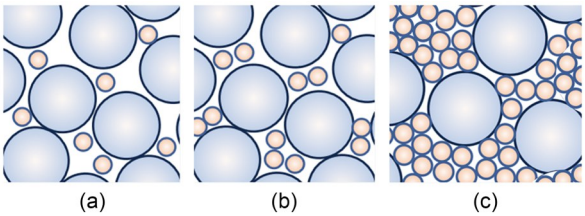

Fig. 11 Schematic representation of binary granular mixtures with various fines contents: (a) coarse particle-dominated structure, where fines are present in small amounts, insufficient to fill the voids between coarse particles; (b) binary granular mixtures at the lower transitional threshold; (c) fine particle-dominated structure, where coarse grains are scarce, embedded within a matrix dominated by fine particles

As f_c increases, η_r^f generally decreases. This trend can be divided into three distinct phases (Fig. 9): Stage I, a steep decline; Stage II, a continued decline with a slight change in slope; Stage III, a gentle reduction. These phases reflect the structural transition of the binary packing system from coarse to fine particle dominance (Fig. 11). At low f_c, many fine particles remain unjammed in voids between coarse particles (Fig. 11a), leading to a sharp initial drop in η_r^f (Stage I) as voids begin to fill. When f_c reaches a lower transitional fines content (indicated by the red dashed lines in Fig. 9), many fine particles remain unjammed. A small increase in f_c causes a large fraction of these particles to jam simultaneously (Fig. 11b), leading to another significant decrease in η_r^f (Stage II). Eventually, beyond the upper transitional threshold (red dotted lines in Fig. 9), most voids become saturated, and most fine particles attain mechanical stability (Fig. 11c), resulting in a slow decrease in η_r^f (Stage III).

It is important to clarify the definitions used for the transitional fines content. In Fig. 5, the threshold or transitional fines content f_c^{th} is identified as the point at which the trend reverses. In contrast, Fig. 9 defines the lower and upper transitional fines contents as the two inflection points in the η_r^f–f_c curve, which delineates the transitional zone. Both the transitional fines contents and the width of the transitional zone vary with the size ratio α (Fig. 12). Specifically, the lower threshold tends to decrease with increasing α, whereas the upper threshold generally increases. An exception occurs at α=9, where the upper threshold appears unusually high—likely due to the relatively sparse experimental coverage near the upper transitional range, as indicated by the wide spacing between tested fines contents in this region, which limited the accuracy of upper threshold identification. Although the comparative analyses for α=12 and 16 are discussed in Section 3.2, their data are also included in Fig. 12 for completeness.

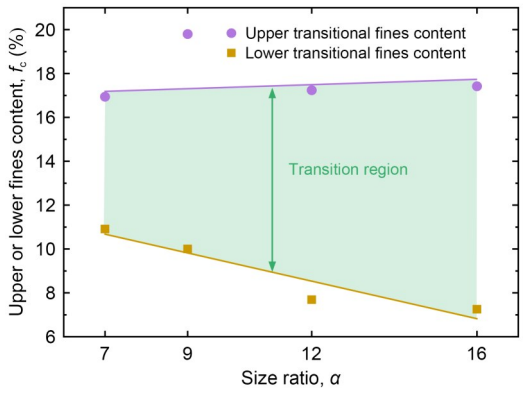

Fig. 12 Lower and upper transitional fines contents as a function of α

3.2 Comparison with DEM simulations

To further validate the proposed MCS-based method, DEM simulations were carried out on binary mixtures with four size ratios (α=7, 9, 12, and 16) subjected to isotropic biaxial compression.

3.2.1 Simulation setup and procedure

DEM simulations were conducted using PFC2D (Itasca Consulting Group, Inc., USA), employing a linear contact model governed by Coulomb friction (Hu et al., 2024; Ling et al., 2024). The model can be expressed as follows:

$$\begin{cases} f_{\mathrm{n}} = k_{\mathrm{n}}\delta_{\mathrm{n}}, \\ f_{\mathrm{s}} = \min\{f_{\mathrm{s0}} + k_{\mathrm{s}}\Delta\delta_{\mathrm{s}}, \mu f_{\mathrm{n}}\}, \end{cases} \tag{3}$$

where f_{n} and f_{s} are the normal and tangential contact forces, respectively; k_{n} and k_{s} are the corresponding normal and tangential contact stiffnesses, respectively; f_{s0} is the initial tangential force at the current time step; δ_{n} represents the normal overlap between particles; $\Delta\delta_{\mathrm{s}}$ is the incremental tangential displacement; μ is the interparticle frictional coefficient. This contact model enables a detailed analysis of both particle–particle and particle–wall interactions (Navarro and de Souza Braun, 2013).

The simulation consists of two stages: sample generation and isotropic loading (Fig. 13). For sample generation, following the criteria of Shire et al. (2014) and Indraratna et al. (2022), each sample contained more than 500 coarse particles to ensure representativeness. The particles were randomly distributed within a square domain bounded by frictionless rigid walls. After the initial configuration was established, an isotropic compression protocol was applied by slowly moving the walls inward under a constant confining pressure of 100 kPa. Compression continued until the system reached mechanical equilibrium, defined by contact force fluctuations below 1×10^{-5} (Yang and Chu, 2024). Gravity was neglected during the entire process to avoid particle segregation and anisotropy. The representative compositions of the mixtures used in the simulations are presented in Table 3, and a complete list of all simulation cases is provided in Section S2 of the ESM. Fine particles with less than three contacts were identified as rattlers, following the convention of previous studies (Babu et al., 2023; Newhall, 2025; Petit and Sperl, 2025).

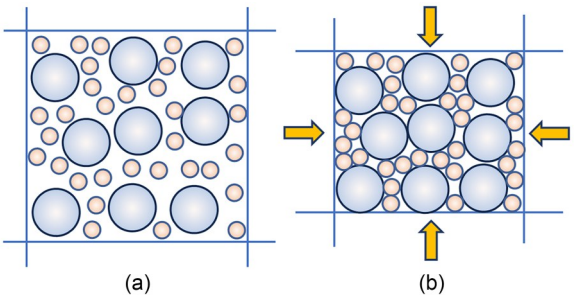

Fig. 13 Schematic diagram of the DEM simulation: (a) sample generation; (b) isotropic compression

Table 3 Representative DEM simulation cases for different size ratios

Size ratio, α	Fines content, f_{c} (%)	Number of particles
7	2.00	4172
	7.55	10463
	19.67	7883
	24.62	10183
	30.99	17066
	44.94	22837
9	1.22	4382
	7.95	11818
	14.74	7815
	33.06	27921
	46.36	39121
12	1.37	3348
	11.11	19114
	21.74	32773
	33.33	44614
	38.46	57199
16	1.54	12536
	10.49	19003
	21.47	41251
	30.43	66331
	40.19	72474

3.2.2 Parameter calibration and model validation

To ensure the fidelity of the DEM model, the contact parameters were calibrated by matching the simulated fine-rattler fraction to the experimental observations. The normal contact stiffness k_{n} can be derived from the effective modulus E^* using the relation $k_{\mathrm{n}}=AE^*/L$, where A=2R, R=min$\{R^{(1)}, R^{(2)}\}$, and $L=R^{(1)}+R^{(2)}$ (Itasca Consulting Group, Inc., 2014; Meshkinghalam et al., 2025). Here, $R^{(1)}$ and $R^{(2)}$ denote the radii of the

two particles in contact. The final calibrated parameters are listed in Table 4. Fig. 14 presents a comparison of the fine rattler fraction η_r^f obtained from the DEM and experimental measurements for binary mixtures with α=7 and 9, showing good agreement and validating the accuracy of the calibrated model.

Table 4 Parameters used in the numerical simulation

Parameter	Value
Normal contact stiffness of walls (N/m)	1×10^9
Effective modulus (Pa)	1×10^8
Confining pressure (kPa)	100
Stiffness ratio (k_n/k_s)	1.0
Interparticle frictional coefficient	0.0
Wall–particle frictional coefficient	0.0
Particle density (kg/m^3)	2650
Damping coefficient	0.7

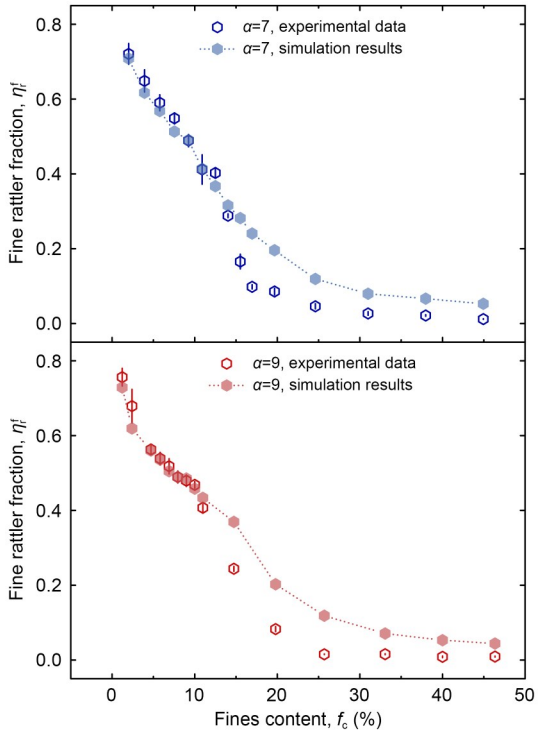

Fig. 14 Comparison of simulated and experimental fine rattler fraction for size ratios (α=7 and 9). Error bars indicate one standard error of the mean

3.2.3 Comparison with MCS predictions

Fig. 15 shows η_r^f obtained from DEM simulations for various f_c values at α=7, 9, 12, and 16. The MCS-based predictions generally agree with the DEM results, confirming the validity of the proposed method. Although the MCS inputs differ—being derived from experimental measurements for α=7 and 9 and from DEM simulations for α=12 and 16—the predicted trends are consistent across all tested size ratios, indicating that the method's performance is robust to the source of size and positional information of the coarse particles. At low f_c, the MCS slightly overestimates η_r^f, mainly due to its idealized rattler identification criterion. In contrast, at high f_c, the MCS tends to underestimate η_r^f, likely due to the mechanism inherent to the MCS method: a higher f_c (or equivalently, a lower fraction of coarse particles) leads to larger but fewer adjusted void circles. This mechanism is illustrated in Fig. 16 using an area-equivalent example based on adjusted void circles: a system with three voids, each accommodating up to three fine particles (N_3=3), has the same total void area as one void holding nine particles (N_9=1). When 10 fine particles are distributed into these systems, the multiple-void configuration is more likely to leave some voids underfilled, producing rattlers (e.g., two in Fig. 16a), whereas the single large void can accommodate all particles without generating rattlers (Fig. 16b).

In summary, at high f_c, the MCS method's idealized assumptions tend to overestimate η_r^f, while the reduced number of voids due to fewer coarse particles—despite being larger—introduces an underestimation effect. These opposing mechanisms compete, and our results suggest that the underestimation effect dominates, resulting overall in a lower MCS-predicted η_r^f compared to DEM. In contrast, at low f_c, the underestimation mechanism becomes negligible, and the overestimation due to idealized assumptions prevails.

In addition, Fig. 17 presents quantitative comparisons between DEM simulations and MCS predictions. The L_2 norm remains below 0.07, the mean error (ME) below 0.06, and the maximum error (MaxE) below 0.12, indicating small deviations across all cases. Detailed definitions of the three error metrics can be found in Section S1 of the ESM.

4 Discussion

The proposed MCS-based approach requires the sizes and spatial positions of coarse particles as known inputs. For validation, coarse particle data were obtained from both experiments and DEM simulations

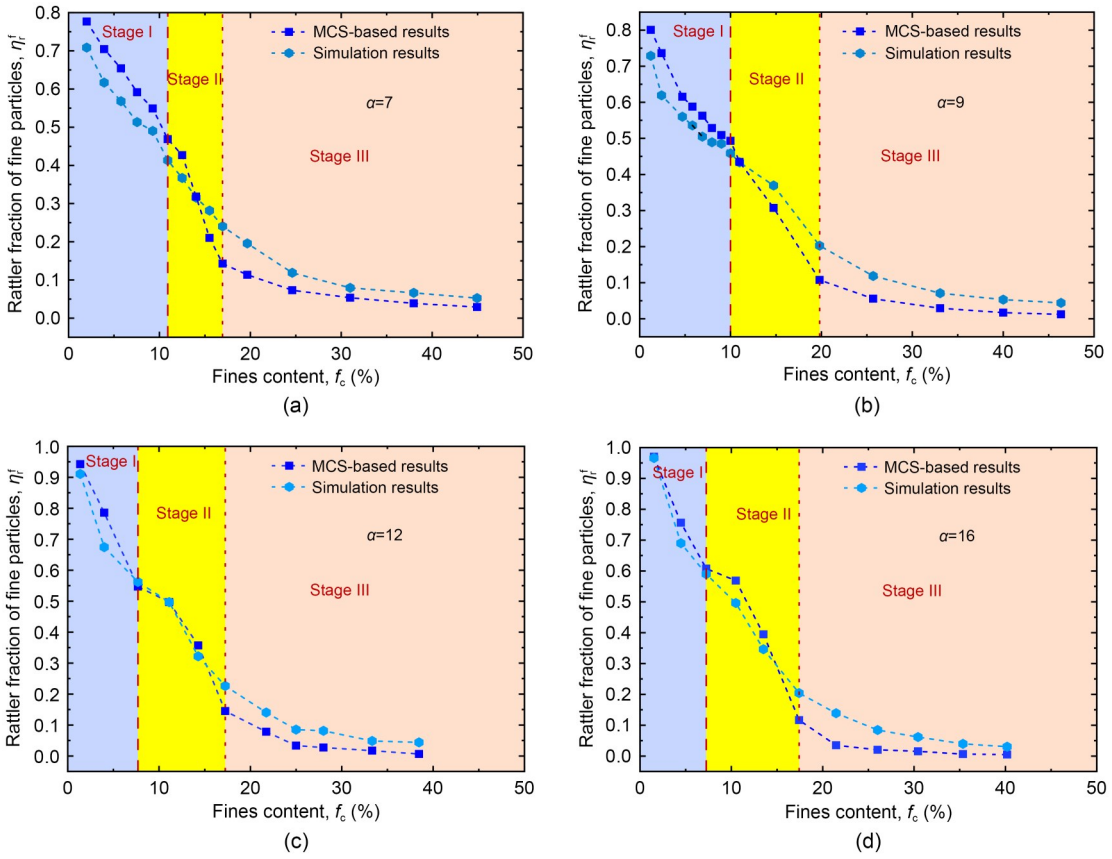

Fig. 15 Comparison of MCS-based and simulated rattler fractions for the four size ratios: (a) α=7; (b) α=9; (c) α=12; (d) α=16. For α=7 and 9, the MCS-based results are from Fig. 9, and the DEM results are from Fig. 14

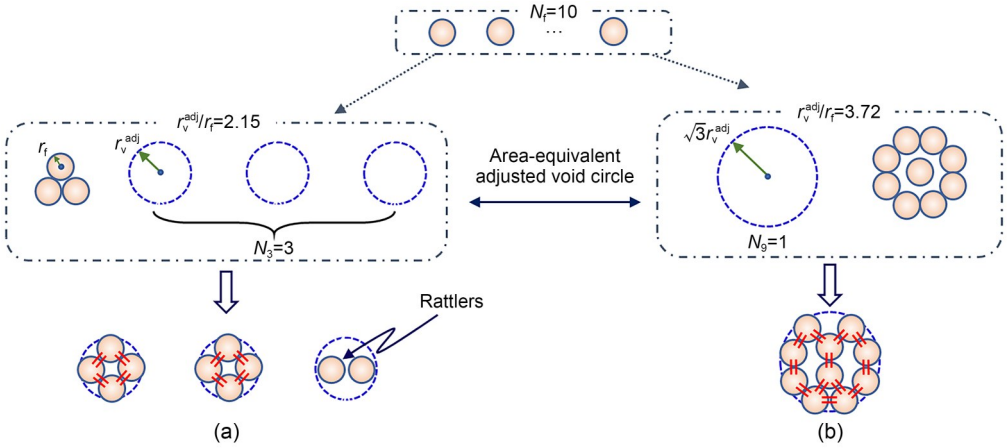

Fig. 16 Schematic of the underestimation mechanism of the MCS method at a high fines content: (a) multiple small voids leading to underfilled voids and rattlers; (b) a single large void accommodating all particles with no rattlers, despite an equal total void area in both cases. The dashed circle represents the adjusted void circle, while short red double-solid lines denote contacts between particles and their neighbors

in this study. Granular packings are generally generated by two approaches: dynamic methods (Cundall and Strack, 1979; Ting et al., 1993), such as DEM, which solve the equations of particle motion, and geometric methods (Feng et al., 2003; Bagi, 2005), which construct packings purely through geometric calculations. Representative geometric methods include the inward packing method (Bagi, 2005) and the advancing front

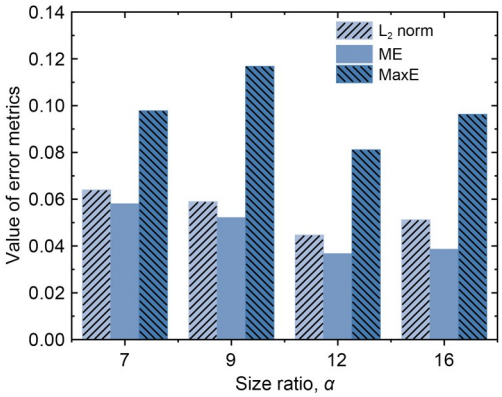

Fig. 17 Error comparison for different size ratios (α=7, 9, 12, and 16)

approach (Feng et al., 2003). Compared with dynamic methods, geometric approaches are more computationally efficient and can rapidly generate large numbers of packings. However, they typically yield relatively dense configurations and face challenges in reproducing different void ratios under the same particle size distribution.

Overall, geometric methods provide a reliable means of obtaining coarse particle configurations for estimating η_r^f in dense packings. For looser systems, η_r^f may instead be approximated by fitting a functional relationship between its values in dense packings and the void ratio e. Although geometric methods were not directly applied in this study, they hold strong potential for extending the applicability of the MCS framework and warrant further investigation.

In addition, although the present study was restricted to 2D granular systems, the MCS-based framework is conceptually extendable to 3D packings. In this case, the void identification step can be adapted using 3D Delaunay tessellation to construct inscribed void spheres that are tangent to the four particles located at the vertices of each Delaunay tetrahedron. These inscribed spheres can then be adjusted based on the 3D maximum packing density to determine the maximum number of fine particles that can be placed within each void. The fine particle capacity in each void is directly determined from the best known packings of equal spheres in a sphere (Otto von Guericke University Magdeburg, 2025b). Finally, fine particles are randomly assigned to the classified pore spheres, with their initial weights and update procedures following the same approach described in Section 2.4. The MCS is repeated multiple times to obtain statistically stable results.

5 Conclusions

In this paper, we designed a MCS-based method for estimating the fine rattler fraction η_r^f in large-ratio binary mixtures. Its performance and potential limitations were examined by comparing predictions with experimental measurements and DEM simulations. Based on these analyses, we drew the following conclusions:

(1) The MCS-based predictions closely matched the experimental results for mixtures with α=7 and 9, showing a slight overall overestimation. This deviation stems mainly from the idealized assumption of the maximum void capacity and is attributed partly to the contact detection criterion used in experimental image processing. At low f_c, the MCS-based predictions tend to overestimate η_r^f compared to DEM results, mainly due to its idealized identification assumptions. However, as f_c increases, the trend reverses, and η_r^f is underestimated. This is likely because the reduction in the number of adjusted void circles—resulting from a lower proportion of coarse particles—has a stronger underestimation effect than the overestimation induced by the idealized assumption, leading to an overall underprediction of η_r^f at high f_c.

(2) Two transitional points in the η_r^f–f_c curve, identified by inflection points in the slope, delineate three distinct phases: (I) a steep initial decline, (II) a continued decline with a slight change in the slope, and (III) a final gentle decrease. As α increases, the lower transitional fine content shifts downward, while the upper transitional content tends to shift upward.

(3) Although the present study focused on 2D granular assemblies for their geometric simplicity, the developed MCS framework provides a conceptual and computational foundation for extension to more realistic 3D packings, including void identification via Delaunay tetrahedron and fine particle allocation within inscribed pore spheres.

(4) The assumption of circular particles in this study simplifies the representation of granular materials. To enhance the practical relevance of the proposed methods, future work should aim to incorporate particle shape irregularities and multicomponent mixtures.

In summary, the proposed MCS method enables robust and relatively accurate estimation of the fine particle rattler fraction η_r^f using only the size and positional information of coarse particles. This framework advances both experimental analysis and theoretical

modeling in granular physics and provides a foundation for extending the approach to more complex 3D granular systems.

Acknowledgments

This work is supported by the National Natural Science Foundation of China (No. 51988101).

Author contributions

Jing WANG and Daosheng LING contributed to the conceptualization, formal analysis, and investigation. Jing WANG and Changyu SHI contributed to the methodology. Daosheng LING provided the supervision and funding acquisition. Jing WANG wrote the first draft of the manuscript. All authors read and approved the final version.

Conflict of interest

Jing WANG, Changyu SHI, and Daosheng LING declare that they have no conflict of interest.

References

Al-Raoush R, Thompson K, Willson CS, 2003. Comparison of network generation techniques for unconsolidated porous media. *Soil Science Society of America Journal*, 67(6): 1687-1700. https://doi.org/10.2136/sssaj2003.1687

Babu V, Vinutha HA, Bi DP, et al., 2023. Discontinuous rigidity transition associated with shear jamming in granular simulations. *Soft Matter*, 19(48):9399-9404. https://doi.org/10.1039/D3SM00725A

Bagi K, 2005. An algorithm to generate random dense arrangements for discrete element simulations of granular assemblies. *Granular Matter*, 7(1):31-43. https://doi.org/10.1007/s10035-004-0187-5

Behringer RP, Chakraborty B, 2019. The physics of jamming for granular materials: a review. *Reports on Progress in Physics*, 82(1):012601. https://doi.org/10.1088/1361-6633/aadc3c

Berzi D, Vescovi D, 2021. Cooling after shearing: three possible fates for dense granular materials. *Granular Matter*, 23(2):47. https://doi.org/10.1007/s10035-021-01102-9

Biazzo I, Caltagirone F, Parisi G, et al., 2009. Theory of amorphous packings of binary mixtures of hard spheres. *Physical Review Letters*, 102(19):195701. https://doi.org/10.1103/PhysRevLett.102.195701

Bryant SL, King PR, Mellor DW, 1993. Network model evaluation of permeability and spatial correlation in a real random sphere packing. *Transport in Porous Media*, 11(1): 53-70. https://doi.org/10.1007/BF00614635

Cheng Z, Wang JF, 2018. Experimental investigation of interparticle contact evolution of sheared granular materials using X-ray micro-tomography. *Soils and Foundations*, 58(6):1492-1510. https://doi.org/10.1016/j.sandf.2018.08.008

CGAL (The Computational Geometry Algorithms Library), 2024. CGAL 6.1–Manual. https://doc.cgal.org/latest/Manual/packages.html

Cundall PA, Strack ODL, 1979. A discrete numerical model for granular assemblies. *Géotechnique*, 29(1):47-65. https://doi.org/10.1680/geot.1979.29.1.47

Duverger S, Duriez J, Philippe P, et al., 2021. Rattlers' involvement for possibly looser critical states under higher mean stress. *EPJ Web of Conferences*, 249:11002. https://doi.org/10.1051/epjconf/202124911002

Elishakoff I, 2003. Notes on philosophy of the Monte Carlo method. *International Applied Mechanics*, 39(7):753-762. https://doi.org/10.1023/A:1026236621486

Feng YT, Han K, Owen DRJ, 2003. Filling domains with disks: an advancing front approach. *International Journal for Numerical Methods in Engineering*, 56(5):699-713. https://doi.org/10.1002/nme.583

Gao GH, Li DQ, Cao ZJ, 2023. Identification of the design point based on Monte Carlo simulation. *Computers and Geotechnics*, 159:105438. https://doi.org/10.1016/j.compgeo.2023.105438

Hu TT, Ling DS, Tang Y, et al., 2024. Evolution of rattlers under different confining pressures and its influence on shear strength. *Transportation Geotechnics*, 44:101176. https://doi.org/10.1016/j.trgeo.2023.101176

Hu Y, Wang Y, 2020. Probabilistic soil classification and stratification in a vertical cross-section from limited cone penetration tests using random field and Monte Carlo simulation. *Computers and Geotechnics*, 124:103634. https://doi.org/10.1016/j.compgeo.2020.103634

Huang X, Hanley KJ, O'Sullivan C, et al., 2014. Exploring the influence of interparticle friction on critical state behaviour using DEM. *International Journal for Numerical and Analytical Methods in Geomechanics*, 38(12):1276-1297. https://doi.org/10.1002/nag.2259

Hurley RC, Lim KW, Ravichandran G, et al., 2016a. Dynamic inter-particle force inference in granular materials: method and application. *Experimental Mechanics*, 56(2):217-229. https://doi.org/10.1007/s11340-015-0063-8

Hurley RC, Hall SA, Andrade JE, et al., 2016b. Quantifying interparticle forces and heterogeneity in 3D granular materials. *Physical Review Letters*, 117(9):098005. https://doi.org/10.1103/PhysRevLett.117.098005

Indraratna B, Haq S, Rujikiatkamjorn C, et al., 2022. Microscale boundaries of internally stable and unstable soils. *Acta Geotechnica*, 17(5):2037-2046. https://doi.org/10.1007/s11440-021-01321-7

Itasca Consulting Group, Inc., 2014. PFC—Particle Flow Code, Ver. 5.0. Itasca, Minneapolis, USA.

Jiang HR, Kawamoto R, Matsushima T, 2024. Exploring the combined effect of particle shape and friction on cell structures in granular packings via LS-DEM modeling. *IOP Conference Series: Earth and Environmental Science*, 1330(1):012047. https://doi.org/10.1088/1755-1315/1330/1/012047

Kumar N, Magnanimo V, Ramaioli M, et al., 2016. Tuning the bulk properties of bidisperse granular mixtures by small

amount of fines. *Powder Technology*, 293:94-112. https://doi.org/10.1016/j.powtec.2015.11.042

Kwan AKH, Chan KW, Wong V, 2013. A 3-parameter particle packing model incorporating the wedging effect. *Powder Technology*, 237:172-179. https://doi.org/10.1016/j.powtec.2013.01.043

Lade P, Liggio C, Yamamuro J, 1998. Effects of non-plastic fines on minimum and maximum void ratios of sand. *Geotechnical Testing Journal*, 21(4):336-347. https://doi.org/10.1520/gtj11373j

Lee CL, Bililign E, Azéma E, et al., 2025. Loading-dependent microscale measures control bulk properties in granular material: an experimental test of the stress-force-fabric relation. *Physical Review E*, 112(3):035401. https://doi.org/10.1103/rv25-lqdc

Lee K, Hurley RC, 2025. Interplay between forces, particle rearrangements, and macroscopic stress fluctuations in sheared two-dimensional granular media. *Physical Review E*, 112(1):015413. https://doi.org/10.1103/6mh5-7kqd

Li J, Wang D, 2023. Comparison of PDEM and MCS: accuracy and efficiency. *Probabilistic Engineering Mechanics*, 71: 103382. https://doi.org/10.1016/j.probengmech.2022.103382

Li RD, Yin ZY, He SH, 2025. 3D reconstruction of arbitrary granular media utilizing vision foundation model. *Applied Soft Computing*, 169:112599. https://doi.org/10.1016/j.asoc.2024.112599

Lin MC, Wang GQ, Zhou J, et al., 2023. Discrete element method study of hysteretic behavior and deformation characteristics of rockfill material under cyclic loading. *Journal of Zhejiang University-SCIENCE A*, 24(4):350-365. https://doi.org/10.1631/jzus.A2200286

Ling DS, Hu TT, Wang J, et al., 2024. Numerical study on the shear strength of granular materials under the low confining pressure. *Soils and Foundations*, 64(3):101447. https://doi.org/10.1016/j.sandf.2024.101447

Maher CE, Torquato S, 2024. Hyperuniformity scaling of maximally random jammed packings of two-dimensional binary disks. *Physical Review E*, 110(6):064605. https://doi.org/10.1103/PhysRevE.110.064605

Majmudar TS, Sperl M, Luding S, et al., 2007. Jamming transition in granular systems. *Physical Review Letters*, 98(5): 058001. https://doi.org/10.1103/PhysRevLett.98.058001

Meshkinghalam H, Emami Tabrizi M, Chenaghlou MR, 2025. Influence of the contact model on energy fluctuations in non-cohesive granular materials subjected to confinement axial cyclic loading using DEM. *Granular Matter*, 27(1):15. https://doi.org/10.1007/s10035-024-01478-4

Navarro HA, de Souza Braun MP, 2013. Determination of the normal spring stiffness coefficient in the linear spring-dashpot contact model of discrete element method. *Powder Technology*, 246:707-722. https://doi.org/10.1016/j.powtec.2013.05.049

Newhall KA, 2025. Sampling the large-dimensional energy landscape of a 2D granular system with the hydra string method. *Soft Matter*, 21(24):4839-4848. https://doi.org/10.1039/D4SM01337A

Nguyen NS, Taha H, Marot D, 2021. A new Delaunay triangulation-based approach to characterize the pore network in granular materials. *Acta Geotechnica*, 16(7):2111-2129. https://doi.org/10.1007/s11440-021-01157-1

Otto von Guericke University Magdeburg, 2025a. The Best Known Packings of Equal Circles in a Circle. http://hydra.nat.uni-magdeburg.de/packing/cci

Otto von Guericke University Magdeburg, 2025b. The Best Known Packings of Equal Spheres in a Sphere. http://hydra.nat.uni-magdeburg.de/packing/ssp/ssp.html

Petit JC, Sperl M, 2025. Additional jamming transition in two-dimensional bidisperse granular packings. *Physical Review Research*, 7(2):L022073. https://doi.org/10.1103/mtcv-dbpd

Prasad I, Santangelo C, Grason G, 2017. Subjamming transition in binary sphere mixtures. *Physical Review E*, 96(5): 052905. https://doi.org/10.1103/PhysRevE.96.052905

Reboul N, Vincens E, Cambou B, 2008. A statistical analysis of void size distribution in a simulated narrowly graded packing of spheres. *Granular Matter*, 10(6):457-468. https://doi.org/10.1007/s10035-008-0111-5

Reboul N, Vincens E, Cambou B, 2010. A computational procedure to assess the distribution of constriction sizes for an assembly of spheres. *Computers and Geotechnics*, 37(1-2): 195-206. https://doi.org/10.1016/j.compgeo.2009.09.002

Redaelli I, di Prisco C, 2019. Three dimensional steady-state locus for dry monodisperse granular materials: DEM numerical results and theoretical modelling. *International Journal for Numerical and Analytical Methods in Geomechanics*, 43(16):2525-2550. https://doi.org/10.1002/nag.2985

Reyes SC, Iglesia E, 1991. Monte Carlo simulations of structural properties of packed beds. *Chemical Engineering Science*, 46(4):1089-1099. https://doi.org/10.1016/0009-2509(91)85102-4

Roblee LHS, Baird RM, Tierney JW, 1958. Radial porosity variations in packed beds. *AIChE Journal*, 4(4):460-464. https://doi.org/10.1002/aic.690040415.

Santos AP, Bolintineanu DS, Grest GS, et al., 2020. Granular packings with sliding, rolling, and twisting friction. *Physical Review E*, 102(3):032903. https://doi.org/10.1103/PhysRevE.102.032903

Shire T, O'Sullivan C, 2016. Constriction size distributions of granular filters: a numerical study. *Géotechnique*, 66(10): 826-839. https://doi.org/10.1680/jgeot.15.P.215

Shire T, O'Sullivan C, Barreto D, et al., 2013. Quantifying stress-induced anisotropy using inter-void constrictions. *Géotechnique*, 63(1):85-91. https://doi.org/10.1680/geot.11.T.020

Shire T, O'Sullivan C, Hanley KJ, et al., 2014. Fabric and effective stress distribution in internally unstable soils. *Journal of Geotechnical and Geoenvironmental Engineering*, 140(12):04014072.

https://doi.org/10.1061/(ASCE)GT.1943-5606.0001184

Srivastava I, Roberts SA, Clemmer JT, et al., 2021. Jamming of bidisperse frictional spheres. *Physical Review Research*, 3(3):L032042. https://doi.org/10.1103/PhysRevResearch.3.L032042

Sufian A, Russell AR, Whittle AJ, et al., 2015. Pore shapes, volume distribution and orientations in monodisperse granular assemblies. *Granular Matter*, 17(6):727-742. https://doi.org/10.1007/s10035-015-0590-0

Tejada IG, Arroyo M, Ciantia M, 2025. Stress field on intermediate length scales during triaxial compression. *Géotechnique*, 75(6):716-731. https://doi.org/10.1680/jgeot.23.00420

Thakur MM, Penumadu D, 2021. Influence of friction and particle morphology on triaxial shearing of granular materials. *Journal of Geotechnical and Geoenvironmental Engineering*, 147(11):04021118. https://doi.org/10.1061/(ASCE)GT.1943-5606.0002634

Thornton C, 2000. Numerical simulations of deviatoric shear deformation of granular media. *Géotechnique*, 50(1):43-53. https://doi.org/10.1680/geot.2000.50.1.43

Ting JM, Khwaja M, Meachum LR, et al., 1993. An ellipse-based discrete element model for granular materials. *International Journal for Numerical and Analytical Methods in Geomechanics*, 17(9):603-623. https://doi.org/10.1002/nag.1610170902

Wang J, Hu TT, Shi CY, et al., 2026. Partial coordination number and contact proportion of densely packed binary random mixtures of quasi-two-dimensional granular materials. *Powder Technology*, 467:121533. https://doi.org/10.1016/j.powtec.2025.121533

Wang Y, 2011. Reliability-based design of spread foundations by Monte Carlo simulations. *Géotechnique*, 61(8):677-685. https://doi.org/10.1680/geot.10.P.016

Wang Y, Cao ZJ, Au SK, 2010. Efficient Monte Carlo simulation of parameter sensitivity in probabilistic slope stability analysis. *Computers and Geotechnics*, 37(7-8):1015-1022. https://doi.org/10.1016/j.compgeo.2010.08.010

Wautier A, Bonelli S, Nicot F, 2019. Rattlers' contribution to granular plasticity and mechanical stability. *International Journal of Plasticity*, 112:172-193. https://doi.org/10.1016/j.ijplas.2018.08.012

Xia CJ, Li JD, Kou BQ, et al., 2017. Origin of noncubic scaling law in disordered granular packing. *Physical Review Letters*, 118(23):238002. https://doi.org/10.1103/PhysRevLett.118.238002

Xu MQ, Guo N, Yang ZX, 2021. Particle shape effects on the shear behaviors of granular assemblies: irregularity and elongation. *Granular Matter*, 23(2):25. https://doi.org/10.1007/s10035-021-01096-4

Yang DZ, Chu XH, 2024. Influence of particle shape on creep and stress relaxation behaviors of granular materials based on DEM. *Computers and Geotechnics*, 166:105941. https://doi.org/10.1016/j.compgeo.2023.105941

Yang S, Lacasse S, Sandven R, 2006. Determination of the transitional fines content of mixtures of sand and non-plastic fines. *Geotechnical Testing Journal*, 29(2):102-107. https://doi.org/10.1520/gtj14010

Yoshii K, Otsuki M, 2025. Mechanical and geometrical properties of jammed weakly cohesive granular materials. *Journal of the Physical Society of Japan*, 94(8):084801. https://doi.org/10.7566/JPSJ.94.084801

Zhang J, Majmudar TS, Tordesillas A, et al., 2010. Statistical properties of a 2D granular material subjected to cyclic shear. *Granular Matter*, 12(2):159-172. https://doi.org/10.1007/s10035-010-0170-2

Zhang L, Gong WP, Li XX, et al., 2022. A comparison study between 2D and 3D slope stability analyses considering spatial soil variability. *Journal of Zhejiang University-SCIENCE A*, 23(3):208-224. https://doi.org/10.1631/jzus.A2100139

Electronic supplementary materials

Sections S1 and S2